PHYSICAL REVIEW RESEARCH **5**, 023082 (2023)

Prototype of a phonon laser with trapped ions

Chen-Yu Lee,[1,2] Kuan-Ting Lin,[1,2] and Guin-Dar Lin[1,2,3,*]
[1]*Department of Physics and Center for Quantum Science and Engineering, National Taiwan University, Taipei 10617, Taiwan*
[2]*Physics Division, National Center for Theoretical Sciences, Taipei 10617, Taiwan*
[3]*Trapped-Ion Quantum Computing Laboratory, Hon Hai Research Institute, Taipei 11492, Taiwan*

(Received 2 March 2023; accepted 14 April 2023; published 8 May 2023)

We propose a tunable phonon laser prototype with a large trapped ion array, where some of the ions are effectively pinned by optical tweezers, thus isolating a subset of ions that mimics an acoustic cavity used as a phonon lasing resonator. The cavity loss can then be controlled by the tweezer strength and the "wall thickness", the number of pinned ions for isolation. We pump the resonator by applying blue-sideband lasers, and investigate the lasing dynamics of the "cavity" motional modes such as threshold behavior, population distribution, the second-order coherence, and linewidth narrowing. This scheme can be generalized to multimode resonators, for which we report the mode competition phenomenon and lasing mode multistability. Our work provides an excellent platform for acoustic quantum state manipulation, paving the way towards phonon-mediated quantum computing, communications, and metrology.

DOI: 10.1103/PhysRevResearch.5.023082

I. INTRODUCTION

Laser technology has been one of the most critical components in contemporary scientific research, industry, and consumer electronics. The remarkable properties of optical lasers, such as quantum coherence and the capability to travel long distances, make them a unique tool in modern quantum engineering and communication applications. Recently, the acoustic analog of lasing phenomena has drawn growing interest. This line of research extends our understanding beyond ordinary quantum optics to other physical degrees of freedom for their mathematical frameworks share essential similarities. Acoustic waves usually have much slower dynamics than light, providing an opportunity to manipulate constituent elements within a period for precise phase control. Furthermore, the interaction between atoms and phonons can be turned on deterministically through state-dependent kicks as in trapped ion quantum computing and simulation [1] while the photon-atom interface usually relies on probabilistic processes. These features make phononic state control and a phonon laser a new playground for quantum computing [2–11], communications [12,13], and metrology [14–20].

The first phonon laser was realized in a trapped ion system driven by optical forces [21], where a single ion presents self-sustained oscillation beyond a threshold gaining energy from optical sources. Since then, many proposals have been studied and demonstrated in similar platforms [22,23] and others such as quantum dots [24–26] and optomechanical systems [26–35]. Many intriguing properties of ordinary lasers have also been reported in phonon systems, including oscillation threshold [21,27,29,30,32,34–36], Poissonian distribution [34], linewidth narrowing [27–29,32,34,36], injection locking [22,23], mode competition [30,35], and phase control [37]. Most of the schemes, however, are based on sophisticated designs of architecture and cannot be easily scaled up to include more modes. The parameters of the lasing resonator are typically fixed upon fabrication, limiting the opportunities of exploring rich phonon physics.

Here, we propose a prototype of a tunable phonon laser based on a large uniform ion crystal and optical tweezers. Such an ion crystal can be constructed in a long Paul trap [38], or microtrap arrays [39–41]. Notably, many proposed schemes with trapped ions have been recently focused on incorporating optical tweezers to introduce extra control for quantum computing and simulation [42–45]. Here, we apply optical tweezers on one or a few ions in a row so that they form a "wall" for acoustic waves. We then consider a small subset of ions being contained by two such walls, forming an effective phonon cavity as shown in Fig. 1(a). Note that, for a uniform ion crystal, the frequency scale characterizing momentum exchange between adjacent ions is $\omega_0 \equiv [e^2/(4\pi\epsilon_0 m d_0^3)]^{1/2}$, obtained by matching the energy scales of local oscillation and mutual Coulomb interaction, where e is the charge carried by an ion of mass m. For ion separation d_0 about a few microns, ω_0 is of order of magnitude about hundreds of kilohertz to a few megahertz. Therefore, the application of optical tweezers of strength larger than ω_0 by about an order of magnitude can significantly modify the motional spectrum [38], resulting in a collection of local modes formed within the "cavity". This remarkable feature allows us to view the system as a phonon laser resonator.

The beauty of this proposed scheme is its simplicity and flexibility of reconfiguration. Note that optical tweezers can be switched on and off easily at a timescale of nanoseconds,

---

[*] Corresponding author: guindarl@phys.ntu.edu.tw

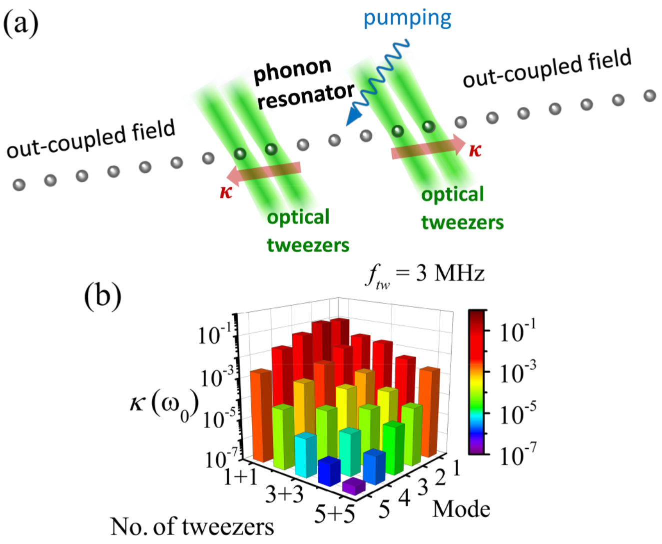

FIG. 1. (a) Architecture of an effective phonon resonator constructed near the middle of a large-scale ion crystal. The tweezered ions act as partial mirrors of the resonator. (b) Mode decay rates against varied wall thickness of an $N_S = 5$ cavity. The collective normal modes are ordered according to their frequencies (1: lowest; 5: highest). These results are calculated based on an $N \approx 2000$ $^{40}\text{Ca}^+$ ion crystal with ion separation 7 μm. The tweezer frequency is $f_{tw} = \omega_{tw}/(2\pi) = 3$ MHz.

without altering the spatial equilibrium of the array. Further, the "cavity size" is scalable on demand. The reflectivity of a partial mirror can be tuned by varying tweezer frequencies and/or numbers of tweezers. In the following discussion, we demonstrate the idea by looking into the lasing dynamics assuming that the ion array is only Doppler cooled.

II. EFFECTIVE PHONON RESONATOR

We consider N_S ions within the effective resonator, and only focus on N_S longitudinal modes. This is because the rest of the array contributes to a bath of a broader dispersion band in the longitudinal modes than the transverse ones. A wall thickness w is represented by the number of tweezered ions. We use $w_L + w_R$ to denote the thicknesses of the left and right walls. Without altering the general conclusion, in this work we look at the symmetric cases with $w_L = w_R$. The number of bath ions is $N_B = N - w_L - w_R - N_S$, where N is the total number of ions. It is assumed that $N_B \gg N_S$ such that the discrete bath spectrum approximates a continuous band and is treated as Markovian.

The motional Hamiltonian is described by $H_m = \sum_i p_i^2/(2m) + \sum_{i,j} A_{ij} z_i z_j$, where z labels the longitudinal direction, z_i is coordinate operator with respect to the equilibrium position of the ith ion, and p_i the associated momentum operator. The coupling matrix elements $A_{ii} = \nu_i^2 + \nu_{tw,i}^2 + \sum_{l=1,l\neq i}^{N} 2/|u_i - u_l|^3$ and $A_{ij} = -2/|u_i - u_j|^3$ for $i \neq j$, where u_i is the equilibrium z position of the ith ion in units of d_0 [46]. Also, $\nu_i = \omega_i/\omega_0$ and $\nu_{tw,i} = \omega_{tw,i}/\omega_0$ are dimensionless frequencies introduced by the global trap and optical tweezers of strength $\omega_{tw,i}$, respectively. Here, we use the trap configuration discussed in [38], a large linear Paul trap with a box-like potential so that $\omega_i \approx 0$ except those near the edges. Our system can be chosen to be anywhere in the middle of the uniform part. We also assume that optical tweezers are applied transversely to the array so $\omega_{tw,i} > 0$ for tweezered ions; otherwise, $\omega_{tw,i} = 0$.

By dividing the whole array into the system C and the bath B, and using the phononic field operator representation, the motional Hamiltonian can be recast into (see Appendix A)

$$H_m = \sum_{q\in C} \hbar\omega_q a_q^\dagger a_q + \sum_{k\in B} \hbar\omega_k a_k^\dagger a_k + \sum_{q\in C,k\in B} g_{qk}(a_q a_k^\dagger + \text{H.c.}), \tag{1}$$

where a_q (a_k) and $a_q^\dagger$ ($a_k^\dagger$) are phononic annihilation and creation operators, respectively, of the qth (kth) normal mode of C (B) with frequency ω_q (ω_k). H.c. stands for the Hermitian conjugate. The system-bath mode coupling $g_{qk} = \frac{\hbar}{2m}\sum_{i\in C,j\in B} U_{C,qi}^T A_{ij} U_{B,jk}/\sqrt{m^2\omega_q\omega_k}$, where the matrices U_C and U_B diagonalize the corresponding submatrices in matrix $\mathbf{A} \equiv [A_{ij}]$. Since $N_B \gg N_S$, the excitation within the cavity can dissipate to the bath's degrees of freedom, and will not revive until the timescale $\sim N_B\omega_0^{-1}$, determined by the elapsed time of motion propagation to the edge and back. Before the revival happens, the dissipation of the cavity modes can be characterized by the decay rates

$$\kappa_q \approx 2\pi \bar{g}_{qq}^2 \rho_B(\omega_q) \tag{2}$$

according to the standard Fermi golden rule approach. Here, we have taken the continuous limit for B and numerically computed the density of states $\rho_B(\omega)$ of the bath. We obtain $\bar{g}_{qq}^2$ by coarse-graining $|g_{qk}|^2$ over a small range of $\omega_k \approx \omega_q$, that is, $\bar{g}_{qq}^2 \equiv \langle |g_{qk}|^2 \rangle_{\omega_k\approx\omega_q}$. Note that this approach is valid as long as the Markovian bath assumption holds. For a large but finite $N \sim \mathscr{O}(10^3)$, we also numerically check the time evolution of the cavity mode population, and extract the decay rates by fitting to an exponential profile. Our results show very good agreement with Eq. (2). See Appendix A for more details. It can be expected that increasing the wall thickness and/or tuning up the tweezer strength enhance isolation of the cavity from the rest of the ion crystal, and therefore decrease the decay rate of the cavity modes. This provides some arbitrariness for system preparation given the state-of-the-art physical constraints [47]. We present the decay rates for an $N_S = 5$ cavity in Fig. 1(b). A typical $\kappa \sim 10^{-3}\omega_0$ implies that one cavity mode survives for about a thousand times of momentum exchanges.

III. SINGLE-MODE PHONON LASING

We now look into the phonon lasing mechanism of a resonator containing only $N_S = 1$ ion, which is pumped by shining optical lasers resonant with the blue sideband. Typically, the cavity mode frequency is about hundreds of kilohertz to a few megahertz, the sidebands are assumed resolvable from the carrier transition by Raman transitions of a few kilohertz in linewidth. We describe the evolution of the system by a master equation

$$\dot{\rho} = -\frac{i}{\hbar}[H_S, \rho] - \sum_{\alpha=\pm} \frac{\kappa_{\mathrm{th}}^{\alpha}}{2} \mathscr{L}_a^{\alpha}[\rho] - \frac{\gamma}{2} \mathscr{L}_{\sigma}^{-}[\rho], \tag{3}$$

where ρ is the system density matrix governed by the system Hamiltonian $H_S/\hbar = -\delta_b \sigma_z/2 + \eta\Omega(a^\dagger \sigma^+ + \sigma^- a)$ in the rotating frame with $\sigma^- = |g\rangle\langle e|$ and $\sigma^+ = |e\rangle\langle g|$ the atomic lowering and raising operators, respectively, between the ground state $|g\rangle$ and excited one $|e\rangle$ separated by energy $\hbar\omega_{eg}$; $\sigma_z = |e\rangle\langle e| - |g\rangle\langle g|$; γ is the natural linewidth; blue sideband detuning $\delta_b \equiv \omega_L - \omega_{eg} - \omega$ with driving laser frequency ω_L and cavity mode frequency ω; η is the Lamb-Dicke parameter; Ω is the Raman Rabi frequency. The Lindblad superoperators are given by $\mathscr{L}_a^{\pm}[\rho] = a^{\pm}a^{\mp}\rho + \rho a^{\pm}a^{\mp} - 2a^{\mp}\rho a^{\pm}$ (here, we denote $a^- = a$ and $a^+ = a^\dagger$ for convenience) and $\mathscr{L}_{\sigma}^{-}[\rho] = \sigma^+\sigma^-\rho + \rho\sigma^+\sigma^- - 2\sigma^-\rho\sigma^+$ with $\kappa_{\mathrm{th}}^{+} = n_{\mathrm{th}}\kappa$ and $\kappa_{\mathrm{th}}^{-} = (n_{\mathrm{th}} + 1)\kappa$, where the noise level n_{th} accounts for nonzero cavity temperature contribution [48] and can be estimated by $n_{\mathrm{th}} = [\exp(\hbar\omega/k_B T) - 1]^{-1}$. Note that the dynamics of the internal states are much faster than the motional ones. We can thus assume that the internal degrees of freedom adiabatically follow the motional operators. The dynamics of the phononic operator is of the form $\dot{a} = (\mathscr{G} - \kappa)a/2 +$ (noise terms), which can be obtained by integrating the Heisenberg equations, with the gain given by

$$\mathscr{G} = \gamma \frac{s}{2}\langle\sigma_z\rangle = \sum_n \frac{\gamma s}{2(1 + ns)} P_n, \tag{4}$$

where $s = 2|\eta\Omega|^2/[\delta_b^2 + (\gamma/2)^2]$. We take $\delta_b = 0$ for simplicity. To determine the population distribution, we recast the master equation (3) into the rate equations (see Appendix A):

$$\begin{aligned} \dot{P}_n = &-[\kappa_{\mathrm{th}}^{-} n + \kappa_{\mathrm{th}}^{+}(n+1)]P_n \\ &+ \kappa_{\mathrm{th}}^{-}(n+1)P_{n+1} + \kappa_{\mathrm{th}}^{+} n P_{n-1} \\ &- \frac{\gamma s}{2}\left(\frac{n+1}{1+ns}P_n - \frac{n}{1+(n-1)s}P_{n-1}\right) \end{aligned} \tag{5}$$

for the probability P_n in the motional n state.

Figure 2(a) shows the gain as a function of pumping strength in the steady state, where we clearly see the lasing behavior with $\mathscr{G}/\kappa \to 1$ as the driving strength $\eta\Omega$ overpasses a threshold $\eta\Omega_c = 0.25\omega_0$. To quantify the degree of lasing, we calculate $\langle n\rangle_s$ and second-order coherence $g^{(2)}(0) \equiv |\langle a^\dagger(0)a^\dagger(\tau)a(\tau)a(0)\rangle/\langle a^\dagger a\rangle^2|_{\tau=0}$. The results are presented in Fig. 2(b). At low pumping level below the threshold, $g^{(2)}(0)$ appears to be around 2 as the phonon number is small, suggesting a thermal chaotic phonon state. When $\eta\Omega > \eta\Omega_c$, the phonon number significantly builds up while the $g^{(2)}$ curve abruptly drops to unity, signaling the emergence of a coherent state, consistent with the gain profile. The steady-state phonon number distribution is also obtained from Eq. (5) and plotted in Fig. 2(c) for various noise levels. At zero temperature, the distribution is exactly Poissonian. The rising noise level gradually broadens the distribution, which becomes super-Poissonian. This is also commonly observed in ordinary optical lasers. We also investigate the linewidth narrowing effect of the lasing mode. The lineshape is given by

$$S(\nu) = \frac{\langle n\rangle_s}{(\nu - \omega)^2 + \Delta\nu^2/4} \tag{6}$$

with $\Delta\nu = \kappa\frac{n_{\mathrm{th}}}{\langle n\rangle_s} + \frac{\gamma}{2\langle n\rangle_s}\frac{s}{1+\langle n\rangle_s s}$ (see Appendix D). One can clearly see from Fig. 2(d) that the spectral linewidth becomes significantly narrowed when $\eta\Omega$ exceeds $\eta\Omega_c = 0.25\omega_0$ due to a drastic increase in the phonon number.

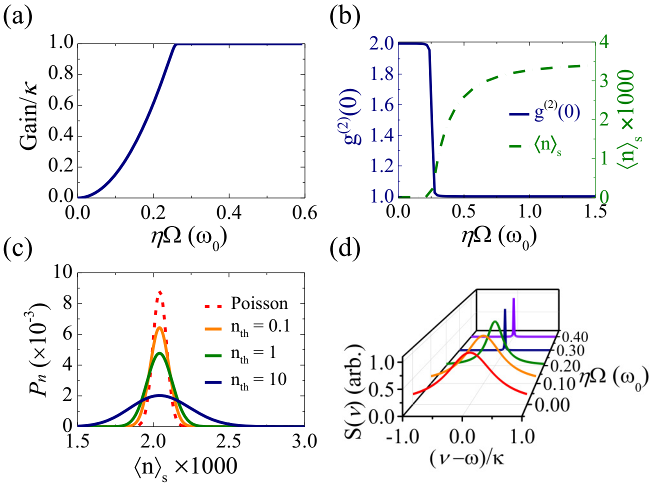

FIG. 2. (a) Gain as a function of driving strength in terms of $\eta\Omega$ on blue sideband resonance $\delta_b = 0$. The lasing threshold is at $\eta\Omega_c = 0.25\omega_0$. (b) Second-order coherence $g^{(2)}$ (left axis) and mean phonon number (right axis) of the cavity mode for varied $\eta\Omega$. (c) Number distribution for $\eta\Omega = 0.4\omega_0 = 2\pi \times 0.2$ MHz with $\langle n\rangle_s = 2200$. The distribution is broadened by increasing the noise level. For comparison, the Poisson distribution ($n_{th} = 0$) is plotted in red dashed line. (d) Spectral lineshape for varied $\eta\Omega$ with the peak value normalized to one. In all cases (a)–(d), we choose $\kappa = 6.1 \times 10^{-3}\omega_0 = 2\pi \times 3.1$ kHz given by 2 + 2 tweezers of frequency $2\pi \times 2.4$ MHz. The cavity mode frequency $\omega = 2.0\omega_0 = 2\pi \times 1.0$ MHz. For (a), (b), and (d), all the results are under the noise level set by the Doppler temperature $n_{\mathrm{th}} = 10$ corresponding to the $^{40}\mathrm{Ca}^+$ ion with natural linewidth $\gamma = 2\pi \times 21.6$ MHz.

IV. MULTIMODE PHONON LASING

We now examine a multi-mode cavity. In the master-equation approach, the computationally involved Hilbert-space grows exponentially with the number of modes as the exponent and with the number of phonon states after truncation as the base. Even for $N_S = 2$, the calculation becomes very demanding for lasing phonon numbers larger than 1000. Fortunately, certain quantities such as mean phonon numbers and correlations can still be obtained by turning to the Heisenberg-Langevin equations considering the quadrature operators $X_q \equiv a_q^\dagger + a_q$ and $P_q \equiv i(a_q^\dagger - a_q)$ for cavity mode q. We leave the detailed derivation in Appendix E and just summarize the results here. Note that this method can be directly adapted to accommodate $N_S > 2$ with minor modifications, for which the results for three and four-mode cases are also presented in Appendix E.

For clarity, we will use the example of $N_S = 2$, where the cavity has two longitudinal collective modes, the center-of-mass (COM) mode and the breathing (BR) mode so $q = \text{COM}$ or BR. We drive the blue-sideband resonances of the cavity modes by applying Raman beams on one of the two ions. Though the two modes (typically separated by several kilohertz) is optically resolvable in experiments, they can exchange energy through common atomic excitation. This can be seen in the gain Eq. (4), where its linewidth is comparable to the atomic one ∼20 MHz, making the result insensitive to the laser detuning.

The system dynamics can be characterized by a parameter corresponding to the classical energy associated with each mode:

$$\mathscr{E}_q(t) \equiv \frac{1}{2}[\langle X_q(t)\rangle^2 + \langle P_q(t)\rangle^2], \tag{7}$$

which in fact approximately corresponds to 2 times of the mean phonon number. We now demonstrate an exemplary case with $w_L + w_R = 1 + 1$ tweezers of frequency $2\pi \times 3$ MHz, yielding $\omega_{\text{COM}} = 1.6\omega_0$ and $\omega_{\text{BR}} = 2.5\omega_0$ with decay rates $\kappa_{\text{COM}} = 0.05\omega_0$ and $\kappa_{\text{BR}} = 0.01\omega_0$, respectively. Here, we have set $\eta = \eta_{\text{COM}}$ the Lamb-Dicke parameter for the COM mode and $\eta_{\text{BR}} = \sqrt{\omega_{\text{COM}}/\omega_{\text{BR}}}\,\eta$ for the BR mode. We then plot the trajectories of $\mathscr{E}_q$ for given lasing parameters starting from an initial state with specific energies $[\mathscr{E}_{\text{COM}}(0), \mathscr{E}_{\text{BR}}(0)]$. Our results show that the two modes cannot sustain lasing simultaneously. The emergence of lasing in one mode with a significant phonon excitation depletes the other mode. To see that, we plot the evolution trajectories of classical energies. Figure 3(a) shows a case where the driving strength is slightly above both thresholds. If we start with an initial state of very low excitation, after a rapid growth and then decrease in the COM mode, the system reaches a steady state of the BR mode exclusively. This is consistent with the single-mode calculation $\eta\Omega_c^{\text{BR}} < \eta\Omega_c^{\text{COM}}$ so the BR mode seems to dominate. When the driving strength becomes sufficiently strong, the system exhibits a bistability where the resultant lasing mode is determined by the initial distribution of excitation between the two modes, as shown in Fig. 3(b).

A phase is then defined by the "macroscopic" excitation of one (lasing) mode. We map out the phase diagrams for various initial classical energies and driving strength. Figure 4 shows the COM and BR phonon number curves, respectively. As the driving strength increases, one can see that the BR mode builds up macroscopically when $\eta\Omega$ exceeds $\eta\Omega_c^{\text{BR}}$. Even when $\eta\Omega$ surpasses $\eta\Omega_c^{\text{COM}}$, the COM mode remains dormant due to cross-mode competition [30]. We meet a sharp-edged threshold at a stronger driving strength $\eta\Omega \approx 1.5\omega_0$, beyond which the COM mode starts to lase and immediately prohibits the BR mode. The discontinuity in phonon numbers signals a first-order phase transition. We also calculate the second-order coherence, and find $g^{(2)}(0) = 1.0$ (≈2.0) for the lasing (nonlasing) mode, consistent with the phase diagram. Such features persist in the three- and four-mode cases (see Appendix F).

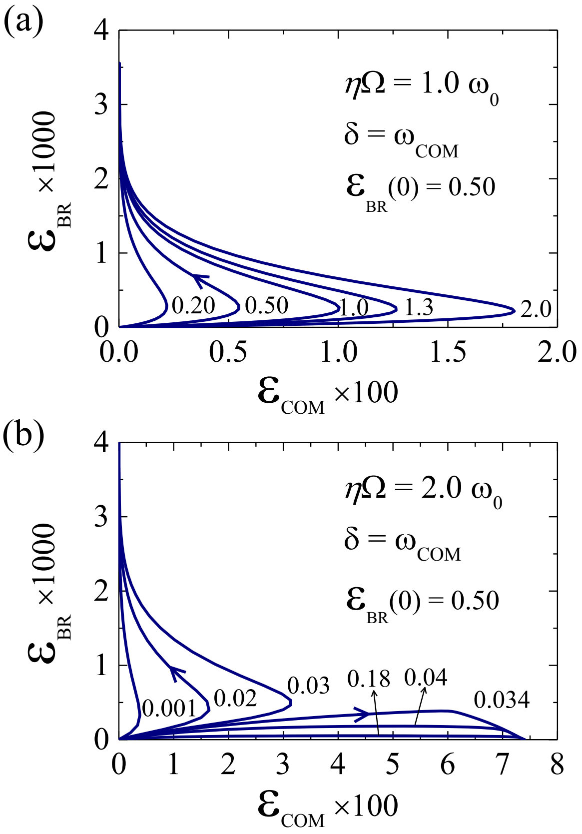

FIG. 3. Temporal classical-energy trajectories showing the evolution of the two modes for (a) $\eta\Omega = 1.0\omega_0$ and (b) $\eta\Omega = 2.0\omega_0$. The destination of each trajectory corresponds to the lasing mode. In (a), every trajectory evolves into the BR mode with $\langle n_{\text{BR}}\rangle_s = 1780$. In (b), depending on the initial distribution of $\mathscr{E}_{\text{BR}}(0)$ and $\mathscr{E}_{\text{COM}}(0)$, the system evolves into the BR mode with $\langle n_{\text{BR}}\rangle_s = 2050$ or the COM mode with $\langle n_{\text{COM}}\rangle_s = 370$. Here, we choose the pump laser to be blue sideband resonant of the COM mode so $\delta = \omega_L - \omega_{eg} = \omega_{\text{COM}}$. The number labeling each trajectory represents $\mathscr{E}_{\text{COM}}(0)$ while $\mathscr{E}_{\text{BR}}(0) = 0.5$ is the same. For reference, the single-mode thresholds are $\eta\Omega_c^{\text{BR}} = 0.4\omega_0$ and $\eta\Omega_c^{\text{COM}} = 0.75\omega_0$.

V. DISCUSSION AND CONCLUSION

We examine the conditions to observe the presented results in an experiment. The feasibility mostly relies on the tweezer strength, the operating temperature, and the finite-size effect. Take $^{40}\text{Ca}^+$ ions for example. It can be shown that the tweezer strength can reach $2\pi \times 3$ MHz with a red-detuning of $2\pi \times 50$ THz, given the state-of-the-art focused beam size of 0.7 μm [47] and a typical laser power 100 mW. Here we only assume the Doppler temperature for the whole array. We find the reported properties can also be observed in a smaller, currently accessible system of $N \approx 100$ under the following consideration: The finite-size nature introduces a non-Markovian effect when the out-coupled wave hits the boundary and rebounces back to the resonator, invalidating our model (see Appendix B). This can be circumvented by only looking at the time span no longer than the time that allows such non-Markovianity to take effect. For instance, it takes about $270 f_0^{-1} \sim 0.5$ ms, shorter than the rebounce time $350 f_0^{-1} \sim 0.7$ ms, where $f_0 = \omega_0/(2\pi)$, to arrive at the steady-state single lasing mode of $\langle n\rangle_s = 334$, corresponding to a displacement of 0.3 μm, significantly larger than 0.05 μm given by thermal noises. In an array of $N \approx 2000$, a steady-state lasing mode of $\langle n\rangle_s \approx 2000$, corresponding to

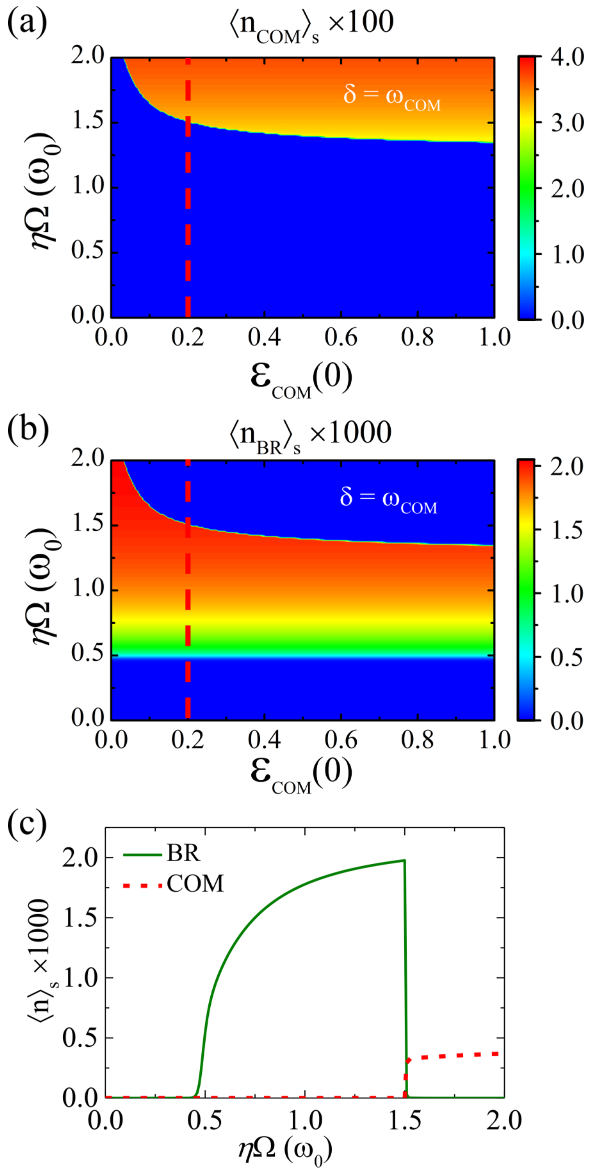

FIG. 4. Steady-state phase diagram in terms of phonon numbers of (a) the COM mode and (b) the BR mode for various $\mathscr{E}_{\rm COM}$ and driving strength $\eta\Omega$. Here, we choose $\mathscr{E}_{\rm BR}(0) = 0.5$ and $\delta = 1.0\omega_{\rm COM}$. The phonon number of the non-lasing mode is comparable to the thermal level $n_{\rm th,COM} = 13$ or $n_{\rm th,BR} = 8.2$. The phonon number of each mode against driving strength is shown in (c), following the line cut in (a) and (b). We find that the BR phase builds up when driving strength surpasses the threshold $\eta\Omega_c^{\rm BR} \approx 0.4\omega_0$, given by the single-mode calculation. A sharp boundary is observed at $\eta\Omega \approx 1.5\omega_0$ (significantly larger than $\eta\Omega_c^{\rm COM} \approx 0.75\omega_0$), beyond which the lasing phase switches to the COM mode.

a displacement of 0.7 μm, takes $2300 f_0^{-1} \sim 4.5$ ms, shorter than the rebounce time $7000 f_0^{-1} \sim 14$ ms. Although such a long array has not been implemented in reality yet, a feasible architecture has been discussed in detail in [38], where the optical tweezers are uniformly distributed to segment the long array for easy stabilization and more efficient cooling. The optical tweezers can then be turned off except those that constitute the partial mirrors for phonon lasing experiments. Laser cooling can be constantly applied to suppress heating of the environment [49] in order to observe the predicted properties.

ACKNOWLEDGMENTS

K.-T.L. and G.-D.L. acknowledge support from NSTC of Taiwan under Projects No. 110-2112-M-002-026, No. 111-2112-M-002-037, and No. 111-2811-M-002-087, and NTU under Project No. NTU-CC-110L890106. G.-D.L. thanks Ming-Shien Chang and Mishkat Bhattacharya for valuable discussion and feedback.

APPENDIX A: DECAY RATES OF CAVITY MODES

In this section we present the detailed calculation of the effective decay rates for the cavity phonon modes. We divide the system into the cavity part (C) and the environment (B) so that the motional Hamiltonian under the harmonic approximation reads

$$H_m = \underbrace{\sum_{i\in C}\frac{p_i^2}{2m} + \sum_{i,j\in C} A_{ij}z_iz_j}_{H_m^C} + \underbrace{\sum_{i\in B}\frac{p_i^2}{2m} + \sum_{i,j\in B} A_{ij}z_iz_j}_{H_m^B} + \underbrace{\sum_{i\in C,j\in B} A_{ij}z_iz_j}_{V_m^{CB}}, \tag{A1}$$

where the elements A_{ij} (see main text) form the coupling matrix $\mathbf{A} = \mathbf{A}_C \oplus \mathbf{A}_B + \mathbf{A}_{CB}$, where $\mathbf{A}_C$ and $\mathbf{A}_B$ are $N_C\times N_C$ and $(N - N_C)\times(N - N_C)$ submatrices describing the coupling within the cavity part and environment, respectively; $\oplus$ denotes the direct sum and $\mathbf{A}_{CB}$ is an $N_C\times(N - N_C)$ matrix containing the interaction between the two subsystems. Each subsystem's coupling matrix can be diagonalized separately to find the normal modes represented by the annihilation and creation operator pair: $(a_q, a_q^\dagger)$ for the cavity part, where the mode index $q = 1, \ldots, N_C$ with $N_C = N_S + w_R + w_L$ the number of ions participating in the cavity and two walls; $(a_k, a_k^\dagger)$ for the environment, where the mode index $k = 1, \ldots, N - N_C$ with N the total number of ions of the entire array. Note that here we also include the tweezered ions in the subsystem C in order to retain the smoothness of the dispersion relation of the bath and secure the Markovianity. However, by doing so, the subsystem C has $w_L + w_R$ more modes than the supposed N_S ones. Fortunately, those $w_L + w_R$ modes mainly resulting from tweezered ions are well separated from the others in frequency, corresponding to spatial wave vectors very localized on the tweezered sites. This allows us to identify the rest as the cavity modes with one-to-one correspondence. In the discussion of phonon lasing, we will only focus on these cavity modes.

Under the rotating wave approximation, the Hamiltonian (A1) can then be rewritten into

$$H_m = \sum_{q=1}^{N_C}\hbar\omega_q a_q^\dagger a_q + \sum_{k=1}^{N-N_C}\hbar\omega_k a_k^\dagger a_k + \sum_{q\in C,k\in B} g_{qk}(a_q a_k^\dagger + a_k a_q^\dagger), \tag{A2}$$

where ω_q and ω_k are the eigenfrequencies of the cavity and environment modes, respectively, and g_{qk} deals with the coupling matrix between mode q in C and mode k in B. Explicitly, $g_{qk} = \frac{\hbar}{2m}\sum_{ij} U^T_{C,qi} A_{ij} U_{B,jk}/\sqrt{m^2\omega_q\omega_k}$ also forms an $N_C \times (N - N_C)$ matrix, where U_C and U_B are the transformation matrices that diagonalize $\mathbf{A}_C$ and $\mathbf{A}_B$, respectively.

The Heisenberg equations of motion for the field operators then read

$$\dot{a}_q = -i\omega_q a_q - i\sum_{k\in B} g_{qk} a_k, \tag{A3}$$

$$\dot{a}_k = -i\omega_k a_k - i\sum_{q\in C} g_{qk} a_q. \tag{A4}$$

By integrating out the bath's degrees of freedom, we obtain the following equation for mode $q \in C$:

$$\begin{aligned}\dot{a}_q =& -i\omega_q a_q - i\sum_{k\in B} g_{qk} a_k(0) e^{-i\omega_k t}\\ &- \sum_{k\in B} |g_{qk}|^2 a_q \int_0^t dt' e^{-i(\omega_k - \omega_q)(t-t')}.\end{aligned} \tag{A5}$$

The second line corresponds to the decay process, which can be characterized by the rate

$$\kappa_q \approx 2\sum_{k\in B} |g_{qk}|^2 \int_0^\infty dt' e^{-i(\omega_k-\omega_q)t'} \approx 2\pi \bar{g}^2_{qq} \rho_B(\omega_q). \tag{A6}$$

For a given finite N, since the cavity and environment degrees of freedom are both discrete and these modes may not overlap, we have calculated the above summation numerically by plugging in the actual parameters. As long as $N \gg N_C$, we find the results have been found to be consistent with the last approximation, where we have taken the continuum limit and numerically computed the density of states $\rho_B(\omega)$ for the bath's degrees, and obtained $\bar{g}^2_{qq}$ by coarse-graining $|g_{qk}|^2$ over a small range of $\omega_k \approx \omega_q$, that is, $\bar{g}^2_{qq} \equiv \langle |g_{qk}|^2 \rangle_{\omega_k \approx \omega_q}$. This amounts to the justification of the validity of the Markov approximation. Also, it should be emphasized that here we only focus on longitudinal modes so that the bath modes constitute a broadband-like spectrum. The approximation breaks down for transverse modes for its extreme narrow-band spectral structure.

To verify our calculation, we also look at the real-time population profile numerically by explicitly including the all motional degrees of the entire array without approximation. As shown in Fig. 5, when the tweezer frequency ω_{tw} is not strong enough compared to ω_0, we find visible large oscillations causing a certain degree of non-Markovianity. Here, $\omega_0 \equiv [e^2/(4\pi\epsilon_0 m d_0^3)]^{1/2}$ is the frequency scale characterizing momentum exchange between adjacent ions separated by d_0, where e is the charge carried by an ion of mass m. But the non-Markovianity can be gradually removed when we increase the tweezer frequency up to approximately an order of magnitude larger than ω_0. In Fig. 5(d), where $\omega_{tw}/\omega_0 = 5.9$, we recover the evolution based on Markovian bath assumption. In this case, we choose $d_0 = 7$ μm for more than 1000 $^{40}\text{Ca}^+$ ions so $\omega_0 = 2\pi \times 0.5$ MHz.

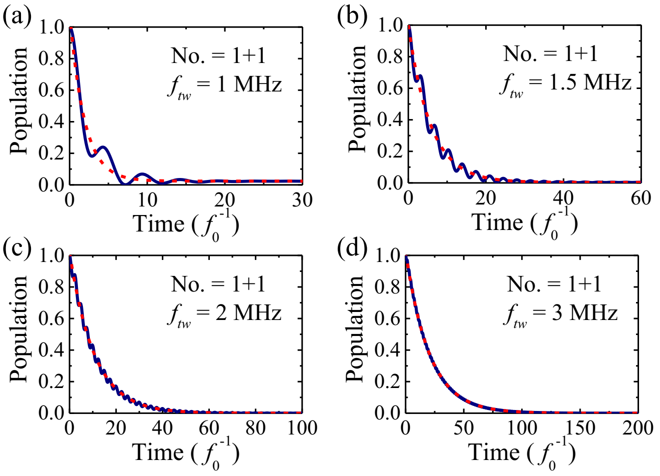

FIG. 5. We show the real-time population profiles (blue curves) of a single-ion resonator given varied tweezer frequencies $f_{tw} = \omega_{tw}/(2\pi)$. These curves are fitted to exponential profiles (red dashed lines) characterized by the decay rates calculated according to Eq. (A6). These results are based on calculation considering an ion crystal of more than 1000 $^{40}\text{Ca}^+$ ions with a uniform separation 7 μm. Here, the unit $f_0 = \omega_0/(2\pi) = 0.5$ MHz.

APPENDIX B: FINITE-SIZE EFFECT

In a more realistic smaller system, the finite size of the system also introduces a non-Markovian effect such that the out-coupled waves hit the boundary and rebounce back to the cavity, which leads to a revival of the local excitation. Fortunately, this can be circumvented if one only looks at the time span no longer than the time that allows such an effect to occur. In the case of $N \approx 100$, we show the excitation dynamics of the cavity mode for longer times in Fig. 6. The revival takes place in about $350 f_0^{-1} \sim 0.7$ ms (rebounce time), where $f_0 = \omega_0/(2\pi) = 0.5$ MHz. To evolve into the steady state of single-mode lasing of $\langle n\rangle_s = 334$, it takes about $270 f_0^{-1} \sim 0.5$ ms, shorter than the rebounce time, leaving a sufficient time difference for measurement. Note that $\langle n\rangle_s = 334$ corresponds to a displacement of 0.3 μm, significantly larger than 0.05 μm given by thermal noises.

We then calculate the relevant lasing properties in this case and plot them in Fig. 7. It can be clear seen that the threshold behavior persists with the critical driving strength

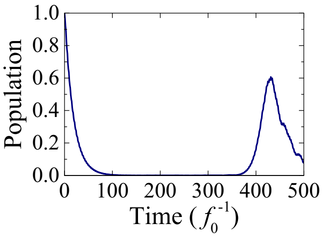

FIG. 6. Relaxation ($0 \sim 100 f_0^{-1}$) and revival (after $350 f_0^{-1}$) of the cavity ion (50th ion) excitation for an array of $N = 100$. Here, we choose $\kappa = 0.056\omega_0 = 2\pi \times 28.3$ kHz given by 1 + 1 tweezers of frequency $2\pi \times 3.0$ MHz. The cavity mode frequency $\omega = 2.0\omega_0 = 2\pi \times 1.0$ MHz.

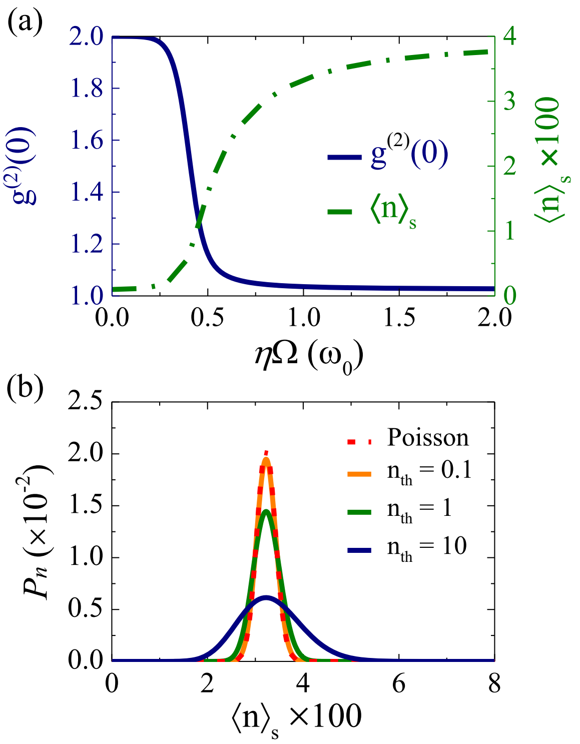

FIG. 7. (a) Second-order coherence $g^{(2)}$ (left axis) and mean phonon number (right axis) of the cavity mode for varied $\eta\Omega$ on an array of $N \approx 100$, under the noise level $n_{\rm th} = 10$ set by the Doppler temperature with a natural linewidth $\gamma = 2\pi \times 21.6$ MHz. (b) Number distributions for varied noise levels corresponding to $\langle n\rangle_s = 334$ with a pumping strength $\eta\Omega = 1\omega_0 = 2\pi \times 0.5$ MHz. Here, we choose $\kappa = 0.056\omega_0 = 2\pi \times 28.3$ kHz given by 1 + 1 tweezers of frequency $2\pi \times 3.0$ MHz. The cavity mode frequency $\omega = 2.0\omega_0 = 2\pi \times 1.0$ MHz.

$\eta\Omega_c = 0.45\omega_0$. The second-order correlation function approaches to a value slightly above unity. The deviation from unity is typically larger in smaller systems than bigger ones. The Poisson number distribution and the broadened profiles by different thermal levels can also be observed.

APPENDIX C: PROBABILITY RATE EQUATION AND GAIN

In this section, we derive the master equation and the corresponding probability rate equations considering the phonon cavity being pumped by blue-sideband lasers. To simplify our discussion, here we only focus on the single mode case with $N_S = 1$ ion. Under the Lamb-Dicke approximation, the Heisenberg equations of motion for the relevant operators are given by

$$\dot{a} = -\frac{\kappa}{2}a - i\eta\Omega\sigma^+, \tag{C1}$$

$$\dot{\sigma}^+ = \left(-i\delta_b - \frac{\gamma}{2}\right)\sigma^+ - i\eta\Omega a\sigma_z, \tag{C2}$$

$$\dot{\sigma}_z = -\gamma(\sigma_z + 1) + 2i\eta\Omega(\sigma^- a - a^\dagger\sigma^+), \tag{C3}$$

where $\sigma^- = |g\rangle\langle e|$ and $\sigma^+ = |e\rangle\langle g|$ are the atomic lowering and raising operators, respectively, between the ground state $|g\rangle$ and excited one $|e\rangle$ separated by energy $\hbar\omega_{eg}$; $\sigma_z = |e\rangle\langle e| - |g\rangle\langle g|$; γ is the natural linewidth; blue side-band detuning $\delta_b \equiv \omega_L - \omega_{eg} - \omega$ with driving laser frequency ω_L and cavity mode frequency ω; η is the Lamb-Dicke parameter; Ω is the Raman Rabi frequency. Note that the dynamics of the internal states are much faster than the motional ones, we can thus assume that the internal degrees of freedom adiabatically follow the motional operators. By taking $\dot{\sigma}^+ \approx 0$, we immediately obtain

$$\sigma^+ \approx -\frac{\eta\Omega a\sigma_z}{\delta_b - i\frac{\gamma}{2}} \tag{C4}$$

and therefore

$$\dot{a} = -\frac{\kappa}{2}a - \frac{1}{2}\frac{\gamma|\eta\Omega|^2}{\delta_b^2 + \left(\frac{\gamma}{2}\right)^2}\sigma_z a + \text{shift} + \text{noise}. \tag{C5}$$

Note that the noise term must be present in order to assure a a valid field operator that satisfies $[a, a^\dagger] = 1$. Both the shift and noise terms are irrelevant for current discussion. The gain can now be identified as

$$\mathscr{G} = -\frac{\gamma|\eta\Omega|^2}{\delta_b^2 + \left(\frac{\gamma}{2}\right)^2}\sigma_z. \tag{C6}$$

Also, by substitution of Eq. (C4) into Eq. (C3) as $\dot{\sigma}_z \approx 0$, we have

$$\sigma_z = -\left(I + \frac{2}{\delta_b^2 + \left(\frac{\gamma}{2}\right)^2}|\eta\Omega|^2 a^\dagger a\right)^{-1} = -\sum_n \frac{1}{1 + ns}|n\rangle\langle n| \tag{C7}$$

and

$$\eta\Omega\sigma^+ = \frac{s}{2}(\delta_b + i\gamma)b, \tag{C8}$$

where $s = \frac{2|\eta\Omega|^2}{\delta_b^2 + (\frac{\gamma}{2})^2}$ and $b \equiv \sum_n \frac{\sqrt{n+1}}{1+ns}|n\rangle\langle n+1|$. Plugging the atomic operators back to the master equation Eq. (3) in the main text, we finally arrive at

$$\begin{aligned}\dot{P}_n = &-\frac{\kappa}{2}(n_{\rm th} + 1)(2nP_n - 2(n+1)P_{n+1})\\ &-\frac{\kappa}{2}n_{\rm th}(2(n+1)P_n - 2nP_{n-1})\\ &-\frac{\gamma s}{2}\left(\frac{n+1}{1+ns}P_n - \frac{n}{1+(n-1)s}P_{n-1}\right).\end{aligned} \tag{C9}$$

Here, we have added the thermal contribution characterized by the noise level $n_{\rm th}$, which can be estimated by $n_{\rm th} = [\exp(\hbar\omega/k_BT) - 1]^{-1}$ [48]. In the steady state, the probability can be computed

$$P_n = P_0\prod_{k=1}^{n}\frac{\kappa n_{\rm th} + \frac{1}{2}\frac{\gamma s}{1+(k-1)s}}{\kappa(n_{\rm th} + 1)} \tag{C10}$$

with P_0 the normalization factor such that $\sum_n P_n = 1$.

APPENDIX D: LINEWIDTH NARROWING

To find out the spectral lineshape of the phonon field, we first look at the mean phonon number equation $d\langle a^\dagger a\rangle/dt =$

$\sum_n n\dot{P}_n$. By substitution of Eq. (C10), we obtain [48]

$$\frac{d}{dt}\langle n\rangle = \sum_n \left\{ \left(\frac{\gamma}{2}\frac{s}{1+n\cdot s} - \kappa \right) nP_n + \left(\kappa n_{\text{th}} + \frac{\gamma}{2}\frac{s}{1+ns} \right) P_n \right\} \approx \left(\frac{\gamma}{2}\frac{s}{1+\langle n\rangle s} - \kappa \right)\langle n\rangle + \kappa n_{\text{th}} + \frac{\gamma}{2}\frac{s}{1+\langle n\rangle s}, \tag{D1}$$

where we have approximated n in the denominator of the summand by its instantaneous mean value $\langle n\rangle$. We thus can identify the gain $\mathscr{G}(t) = \frac{\gamma}{2}\frac{s}{1+\langle n\rangle s}$, consistent with Eq. (C6) except n is taken to be the mean value. In the steady state, $\langle n\rangle \to \langle n\rangle_s$, and

$$\mathscr{G} \to \kappa\left(1 - \frac{n_{\text{th}}}{\langle n\rangle_s}\right) - \frac{\gamma}{2\langle n\rangle_s}\frac{s}{1+\langle n\rangle_s s}. \tag{D2}$$

On the other hand, the Langevin equation reads

$$\dot{a}(t) = \left[\mathscr{G} - \left(\frac{\kappa}{2} + i(\omega - \nu)\right)\right] a(t) + \text{noise terms}, \tag{D3}$$

where ν is the probe frequency understood as a Fourier component. By the quantum regression theorem, we can acquire the spectral lineshape

$$S(\nu) = \mathscr{F}[\langle a^\dagger(\tau)a(0)\rangle] = \frac{\langle n\rangle_s}{(\nu-\omega)^2 + \Delta\nu^2/4} \tag{D4}$$

with $\Delta\nu = \kappa\frac{n_{\text{th}}}{\langle n\rangle_s} + \frac{\gamma}{2\langle n\rangle_s}\frac{s}{1+\langle n\rangle_s s}$, and $\mathscr{F}$ denotes the Fourier transform.

APPENDIX E: HEISENBERG-LANGEVIN FORMALISM OF QUADRATURES

To describe a multimode phonon laser, the master equation (3) in the main text needs to accommodate all modes and their interaction with the atomic state. The Hamiltonian now reads

$$H/\hbar = -\frac{\delta}{2}\sigma_i^z + \sum_q \omega_q a_q^\dagger a_q + \sum_q c_i\eta_q\Omega_i(\sigma_i^+ a_q^\dagger + a_q\sigma_i^-), \tag{E1}$$

where $\delta = \omega_L - \omega_{eg}$; a_q and $a_q^\dagger$ are phonon field operators of the qth cavity mode with frequency ω_q; σ_i^- and σ_i^+ are atomic operators of the ith atom driven by a laser of frequency ω_L and Rabi frequency Ω_i; η_q is the corresponding Lamb-Dicke parameter of the qth mode; c_i is the coefficient determined by the eigenvectors of the system. However, the dimension of the required Hilbert space of the master equation grows exponentially with the number of modes, making the calculation intractable even for $N_S = 2$. Here, we adopt another method based on the normal-mode quadrature operators [35].

We define the normal-mode quadrature operators

$$\begin{cases} X_q = a_q^\dagger + a_q \\ P_q = i(a_q^\dagger - a_q). \end{cases} \tag{E2}$$

Then the Langevin equations of the quadrature operators of different orders are given by

$$\begin{aligned}
\frac{d}{dt}\left(P_q^n X_q^m\right) = {} & -n\omega_q\left(P_q^{n-1}X_q^{m+1} + i(n-1)P_q^{n-2}X_q^m\right) + m\omega_q\left(P_q^{n+1}X_q^{m-1} + i(m-1)P_q^n X_q^{m-2}\right) \\
& -\frac{1}{2}\kappa_q n P_q^n X_q^m + \frac{1}{2}\kappa_q(2n_{\text{th},q}+1)\left(n(n-1)P_q^{n-2}X_q^m\right) - \frac{1}{2}\kappa_q m P_q^n X_q^m + \frac{1}{2}\kappa_q(2n_{\text{th},q}+1)\left(m(m-1)P_q^n X_q^{m-2}\right) \\
& -n\sum_q c_i\eta_q\Omega_i(\sigma_i^- + \sigma_i^+)P_q^{n-1}X_q^m - im\sum_q c_i\eta_q\Omega_i(\sigma_i^- - \sigma_i^+)P_q^n X_q^{m-1},
\end{aligned} \tag{E3}$$

$$\frac{d}{dt}\sigma_i^- = \left(i\delta - \frac{\gamma}{2}\right)\sigma_i^- + i\frac{1}{2}\sum_q c_i\eta_q\Omega_i\sigma_i^z(X_q - iP_q), \tag{E4}$$

$$\frac{d}{dt}\sigma_i^z = -\gamma\left(\sigma_i^z + 1\right) - i\sum_q c_i\eta_q\Omega_i(\sigma_{z,i}^+(X_q - iP_q) - \text{H.c.}). \tag{E5}$$

Note that different modes decay independently but are still coupled through the sharing of atomic states, as revealed by the last terms of Eqs. (E6) and (E7). The second-order coherence can be calculated directly by $g_q^{(2)}(0) = (\langle n_q^2\rangle - \langle n_q\rangle)/\langle n_q\rangle^2$, where

$$\langle n_q\rangle = \frac{1}{4}\left(\langle X_q^2\rangle + \langle P_q^2\rangle\right) - \frac{1}{2} \tag{E6}$$

and

$$\langle n_q^2\rangle = \frac{1}{16}\left(\langle X_q^4\rangle + \langle P_q^4\rangle + 2Re\langle P_q^2 X_q^2\rangle\right) - \frac{1}{4}\left(\langle X_q^2\rangle + \langle P_q^2\rangle + 2Im\langle P_q X_q\rangle + 1\right). \tag{E7}$$

APPENDIX F: MULTIMODE LASING AND MODE COMPETITION

This Heisenberg-Langevin method calculates relevant quadrature-related quantities, such as mean phonon numbers and correlation functions, for multi-mode cases. As the two-mode results have been discussed in the main text, this section presents the results for up to four modes, showing the typical features of mode competition. In the following discussion, we take the parameters given in Tables I and II as examples. We also list the corresponding pumping thresholds obtained from the single-mode model for comparison. As expected, the higher the mode

TABLE I. The mode frequency, decay rate, thermal noise, and threshold for the three-mode cavity.

Mode frequency	Decay rate	Thermal noise	Threshold
$\omega_1 = 1.3\,\omega_0$	$\kappa_1 = 0.05\,\omega_0$	$n_{\mathrm{th},1} = 23$	$0.80\,\omega_0$
$\omega_2 = 2.1\,\omega_0$	$\kappa_2 = 0.01\,\omega_0$	$n_{\mathrm{th},2} = 13$	$0.33\,\omega_0$
$\omega_3 = 2.6\,\omega_0$	$\kappa_3 = 0.005\,\omega_0$	$n_{\mathrm{th},3} = 10$	$0.23\,\omega_0$

TABLE III. The lasing modes with different pumping strengths for three-mode case.

Pumping strength	Lasing mode
$\eta\Omega \lesssim 0.85\,\omega_0$	3rd
$0.85\,\omega_0 \lesssim \eta\Omega \lesssim 2.6\,\omega_0$	2nd or 3rd
$\eta\Omega \gtrsim 2.6\,\omega_0$	All modes

frequency is, the smaller the decay rate, and the lower the threshold.

As in the two-mode cases, we define the classical energy, equivalent to the mode population, to track the evolution of the system:

$$\mathscr{E}_i(t) \equiv \frac{1}{2}[\langle X_i(t)\rangle^2 + \langle P_i(t)\rangle^2] \tag{F1}$$

for the ith normal mode. Determined by the pumping strength $\eta\Omega$, the system evolves into a steady state with one dominant lasing mode, i.e., mode competition. But which lasing mode depends subtly on the choice of the initial $\mathscr{E}_i$. If one, two, three, or more different lasing mode(s) can be found by varying the initial mode populations, the lasing phase is called monostable, bistable, tristable, or multistable, respectively. Figure 8 presents monostable (a), bistable (b), (c), tristable (d)–(f) cases for three cavity modes. The results suggest that the mode with the highest frequency achieves lasing most easily because it has the lowest pumping threshold. But if the initial population of one mode is sufficiently high, it will be forced to lase and suppress other modes. These features remain in the four-mode cases. Tables III and IV provide pumping strength boundaries that separate different multistabilities.

TABLE II. The mode frequency, decay rate, thermal noise, and threshold for the four-mode cavity.

Mode frequency	Decay rate	Thermal noise	Threshold
$\omega_1 = 1.1\,\omega_0$	$\kappa_1 = 0.06\,\omega_0$	$n_{\mathrm{th},1} = 27$	$0.80\,\omega_0$
$\omega_2 = 1.8\,\omega_0$	$\kappa_2 = 0.02\,\omega_0$	$n_{\mathrm{th},2} = 16$	$0.46\,\omega_0$
$\omega_3 = 2.3\,\omega_0$	$\kappa_3 = 0.008\,\omega_0$	$n_{\mathrm{th},3} = 12$	$0.29\,\omega_0$
$\omega_4 = 2.6\,\omega_0$	$\kappa_4 = 0.001\,\omega_0$	$n_{\mathrm{th},4} = 11$	$0.10\,\omega_0$

TABLE IV. The lasing modes with different pumping strengths for four-mode case.

Pumping strength	Lasing mode
$\eta\Omega \lesssim 0.55\,\omega_0$	4th
$0.55\,\omega_0 \lesssim \eta\Omega \lesssim 1.6\,\omega_0$	3rd or 4th
$1.6\,\omega_0 \lesssim \eta\Omega \lesssim 1.8\,\omega_0$	2nd, 3rd, or 4th
$\eta\Omega \gtrsim 1.8\,\omega_0$	All modes

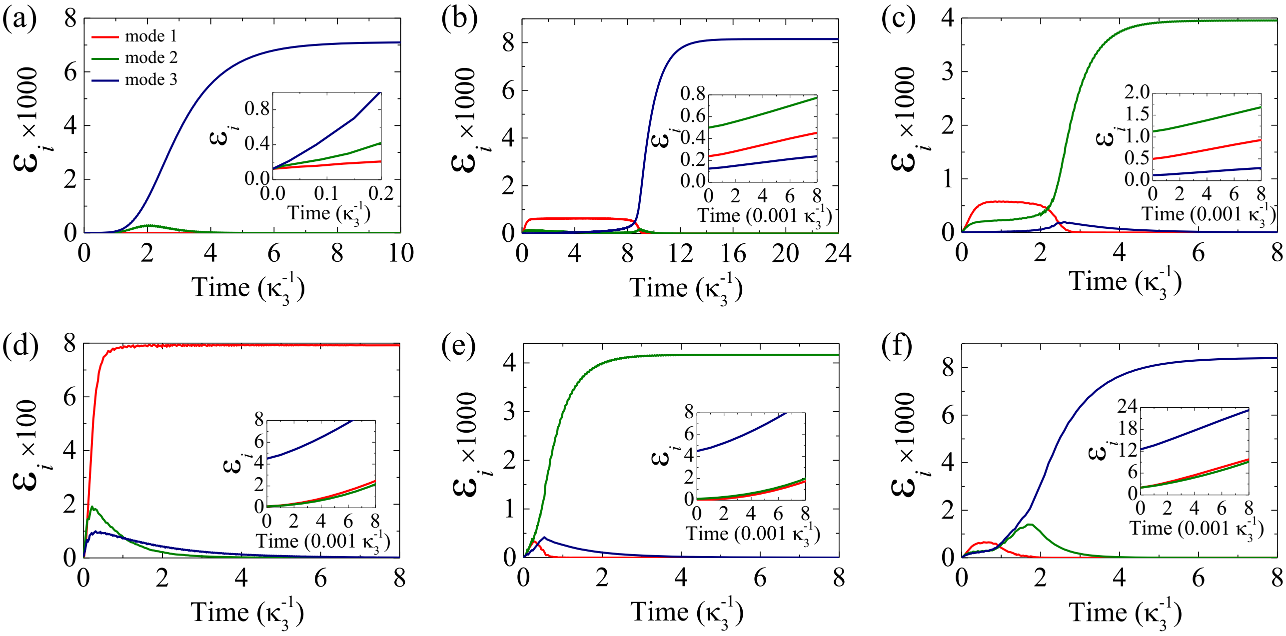

FIG. 8. Classical-energy evolution of the three modes for (a) $\eta\Omega = 0.8\omega_0$, (b), (c) $\eta\Omega = 1.5\omega_0$, (d)–(f) $\eta\Omega = 2.7\omega_0$ with detuning $\delta = \omega_1$. The temporal $\mathscr{E}_{i=1,2,3}$ curves are shown in the inset.

[1] J. I. Cirac and P. Zoller, Quantum Computations with Cold Trapped Ions, Phys. Rev. Lett. **74**, 4091 (1995).

[2] K.-A. B. Soderberg and C. Monroe, Phonon-mediated entanglement for trapped ion quantum computing, Rep. Prog. Phys. **73**, 036401 (2010).

[3] R. Ruskov and C. Tahan, Coherent phonons as a new element of quantum computing and devices, J. Phys.: Conf. Ser. **398**, 012011 (2012).

[4] C. M. Reinke and I. El-Kady, Phonon-based scalable platform for chip-scale quantum computing, AIP Adv. **6**, 122002 (2016).

[5] J. Loye, J. Lages, and D. L. Shepelyansky, Properties of phonon modes of an ion-trap quantum computer in the Aubry phase, Phys. Rev. A **101**, 032349 (2020).

[6] C. Flühmann, T. L. Nguyen, M. Marinelli, V. Negnevitsky, K. Mehta, and J. P. Home, Encoding a qubit in a trapped-ion mechanical oscillator, Nature (London) **566**, 513 (2019).

[7] W. Ge, B. C. Sawyer, J. W. Britton, K. Jacobs, J. J. Bollinger, and M. Foss-Feig, Trapped Ion Quantum Information Processing with Squeezed Phonons, Phys. Rev. Lett. **122**, 030501 (2019).

[8] H. C. J. Gan, G. Maslennikov, K.-W. Tseng, C. Nguyen, and D. Matsukevich, Hybrid Quantum Computing with Conditional Beam Splitter Gate in Trapped Ion System, Phys. Rev. Lett. **124**, 170502 (2020).

[9] C.-H. Nguyen, K.-W. Tseng, G. Maslennikov, H. C. J. Gan, and D. Matsukevich, Quantum-enhanced bosonic learning machine, arXiv:2104.04168.

[10] W. Chen, J. Gan, J.-N. Zhang, D. Matuskevich, and K. Kim, Quantum computation and simulation with vibrational modes of trapped ions, Chin. Phys. B **30**, 060311 (2021).

[11] K. Wan, S. Choi, I. H. Kim, N. Shutty, and P. Hayden, Fault-tolerant qubit from a constant number of components, PRX Quantum **2**, 040345 (2021).

[12] É. Dumur, K. J. Satzinger, G. A. Peairs, M.-H. Chou, A. Bienfait, H.-S. Chang, C. R. Conner, J. Grebel, R. G. Povey, Y. P. Zhong, and A. N. Cleland, Quantum communication with itinerant surface acoustic wave phonons, NPJ Quantum Inf. **7**, 173 (2021).

[13] A. Bienfait, K. J. Satzinger, Y. P. Zhong, H.-S. Chang, M.-H. Chou, C. R. Conner, É. Dumur, J. Grebel, G. A. Peairs, R. G. Povey, and A. N. Cleland, Phonon-mediated quantum state transfer and remote qubit entanglement, Science **364**, 368 (2019).

[14] D. A. R. Dalvit, R. L. de Matos Filho, and F. Toscano, Quantum metrology at the Heisenberg limit with ion trap motional compass states, New J. Phys. **8**, 276 (2006).

[15] C. Sabín, D. E. Bruschi, M. Ahmadi, and I. Fuentes, Phonon creation by gravitational waves, New J. Phys. **16**, 085003 (2014).

[16] D. Hu, L. Niu, S. Jin, X. Chen, G. Dong, J. Schmiedmayer, and X. Zhou, Ramsey interferometry with trapped motional quantum states, Commun. Phys. **1**, 29 (2018).

[17] F. Wolf, C. Shi, J. C. Heip, M. Gessner, L. Pezzè, A. Smerzi, M. Schulte, K. Hammerer, and P. O. Schmidt, Motional Fock states for quantum-enhanced amplitude and phase measurements with trapped ions, Nat. Commun. **10**, 2929 (2019).

[18] M. Drechsler, M. Belen Farías, N. Freitas, C. T. Schmiegelow, and J. P. Paz, State-dependent motional squeezing of a trapped ion: Proposed method and applications, Phys. Rev. A **101**, 052331 (2020).

[19] J. Cerrillo and D. Rodríguez, Motional quantum metrology in a Penning trap, Europhys. Lett. **134**, 38001 (2021).

[20] A. Delakouras, D. Rodríguez, and J. Cerrillo, Production of Fock mixtures in trapped ions for motional metrology, arXiv:2202.00626.

[21] K. Vahala, M. Herrmann, S. Knünz, V. Batteiger, G. Saathoff, T. W. Hänsch, and T. Udem, A phonon laser, Nat. Phys. **5**, 682 (2009).

[22] S. Knünz, M. Herrmann, V. Batteiger, G. Saathoff, T. W. Hänsch, K. Vahala, and T. Udem, Injection Locking of a Trapped-Ion Phonon Laser, Phys. Rev. Lett. **105**, 013004 (2010).

[23] M. Ip, A. Ransford, A. M. Jayich, X. Long, C. Roman, and W. C. Campbell, Phonon Lasing from Optical Frequency Comb Illumination of Trapped Ions, Phys. Rev. Lett. **121**, 043201 (2018).

[24] J. Kabuss, A. Carmele, T. Brandes, and A. Knorr, Optically Driven Quantum Dots as Source of Coherent Cavity Phonons: A Proposal for a Phonon Laser Scheme, Phys. Rev. Lett. **109**, 054301 (2012).

[25] J. Kabuss, A. Carmele, and A. Knorr, Threshold behavior and operating regimes of an optically driven phonon laser: Semiclassical theory, Phys. Rev. B **88**, 064305 (2013).

[26] A. Khaetskii, V. N. Golovach, X. Hu, and I. Žutić, Proposal for a Phonon Laser Utilizing Quantum-Dot Spin States, Phys. Rev. Lett. **111**, 186601 (2013).

[27] I. S. Grudinin, H. Lee, O. Painter, and K. J. Vahala, Phonon Laser Action in a Tunable Two-Level System, Phys. Rev. Lett. **104**, 083901 (2010).

[28] R. P. Beardsley, A. V. Akimov, M. Henini, and A. J. Kent, Coherent Terahertz Sound Amplification and Spectral Line Narrowing in a Stark Ladder Superlattice, Phys. Rev. Lett. **104**, 085501 (2010).

[29] I. Mahboob, K. Nishiguchi, A. Fujiwara, and H. Yamaguchi, Phonon Lasing in an Electromechanical Resonator, Phys. Rev. Lett. **110**, 127202 (2013).

[30] U. Kemiktarak, M. Durand, M. Metcalfe, and J. Lawall, Mode Competition and Anomalous Cooling in a Multimode Phonon Laser, Phys. Rev. Lett. **113**, 030802 (2014).

[31] H. Jing, S. K. Özdemir, X.-Y. Lü, J. Zhang, L. Yang, and F. Nori, $\mathscr{PT}$-Symmetric Phonon Laser, Phys. Rev. Lett. **113**, 053604 (2014).

[32] J. Zhang, B. Peng, Ş. K. Özdemir, K. Pichler, D. O. Krimer, G. Zhao, F. Nori, Y.-X. Liu, S. Rotter, and L. Yang, A phonon laser operating at an exceptional point, Nat. Photon. **12**, 479 (2018).

[33] Y. Jiang, S. Maayani, T. Carmon, F. Nori, and H. Jing, Nonreciprocal phonon laser, Phys. Rev. Appl. **10**, 064037 (2018).

[34] R. M. Pettit, W. Ge, P. Kumar, D. R. Luntz-Martin, J. T. Schultz, L. P. Neukirch, M. Bhattacharya, and A. N. Vamivakas, An optical tweezer phonon laser, Nat. Photon. **13**, 402 (2019).

[35] J. Sheng, X. Wei, C. Yang, and H. Wu, Self-Organized Synchronization of Phonon Lasers, Phys. Rev. Lett. **124**, 053604 (2020).

[36] J. B. Khurgin, M. W. Pruessner, T. H. Stievater, and W. S. Rabinovich, Laser-Rate-Equation Description of Optomechanical Oscillators, Phys. Rev. Lett. **108**, 223904 (2012).

[37] Y.-L. Zhang, C.-L. Zou, C.-S. Yang, H. Jing, C.-H. Dong, G.-C. Guo, and X.-B. Zou, Phase-controlled phonon laser, New J. Phys. **20**, 093005 (2018).

[38] Y.-C. Shen and G.-D. Lin, Scalable quantum computing stabilised by optical tweezers on an ion crystal, New J. Phys. **22**, 053032 (2020).

[39] J. I. Cirac and P. Zoller, A scalable quantum computer with ions in an array of microtraps, Nature (London) **404**, 579 (2000).

[40] A. K. Ratcliffe, R. L. Taylor, J. J. Hope, and A. R. R. Carvalho, Scaling Trapped Ion Quantum Computers Using Fast Gates and Microtraps, Phys. Rev. Lett. **120**, 220501 (2018).

[41] S. Jain, J. Alonso, M. Grau, and J. P. Home, Scalable Arrays of Micro-Penning Traps for Quantum Computing and Simulation, Phys. Rev. X **10**, 031027 (2020).

[42] T. Olsacher, L. Postler, P. Schindler, T. Monz, P. Zoller, and L. M. Sieberer, Scalable and parallel tweezer gates for quantum computing with long ion strings, PRX Quantum **1**, 020316 (2020).

[43] Y. H. Teoh, M. Sajjan, Z. Sun, F. Rajabi, and R. Islam, Manipulating phonons of a trapped-ion system using optical tweezers, Phys. Rev. A **104**, 022420 (2021).

[44] J. D. Arias Espinoza, M. Mazzanti, K. Fouka, R. X. Schüssler, Z. Wu, P. Corboz, R. Gerritsma, and A. Safavi-Naini, Engineering spin-spin interactions with optical tweezers in trapped ions, Phys. Rev. A **104**, 013302 (2021).

[45] M. Mazzanti, R. X. Schüssler, J. D. Arias Espinoza, Z. Wu, R. Gerritsma, and A. Safavi-Naini, Trapped Ion Quantum Computing Using Optical Tweezers and Electric Fields, Phys. Rev. Lett. **127**, 260502 (2021).

[46] S.-L. Zhu, C. Monroe, and L.-M. Duan, Trapped Ion Quantum Computation with Transverse Phonon Modes, Phys. Rev. Lett. **97**, 050505 (2006).

[47] S. Saskin, J. T. Wilson, B. Grinkemeyer, and J. D. Thompson, Narrow-Line Cooling and Imaging of Ytterbium Atoms in an Optical Tweezer Array, Phys. Rev. Lett. **122**, 143002 (2019).

[48] M. S. Pierre Meystre, *Elements of Quantum Optics* (Springer-Verlag, Berlin/Heidelberg, 2007).

[49] G.-D. Lin and L.-M. Duan, Sympathetic cooling in a large ion crystal, Quantum Inf. Process. **15**, 5299 (2016).